

Observation of anomalous thermal Hall effect in altermagnets

Wenbo Wan^{1,2*}, Xu Zhang^{1*✉}, Yixuan Luo³, Yanfeng Guo^{3,4,✉} and Shiyan Li^{1,2,5,6,✉}

¹*State Key Laboratory of Surface Physics, and Department of Physics, Fudan University, Shanghai 200438, China*

²*Shanghai Research Center for Quantum Sciences, Shanghai 201315, China*

³*State Key Laboratory of Quantum Functional Materials, School of Physical Science and Technology, ShanghaiTech University, Shanghai 201210, China*

⁴*ShanghaiTech Laboratory for Topological Physics, ShanghaiTech University, Shanghai 201210, China*

⁵*Shanghai Branch, Hefei National Laboratory, Shanghai 201315, China*

⁶*Collaborative Innovation Center of Advanced Microstructures, Nanjing 210093, China*

Corresponding author. Email: shiyan_li@fudan.edu.cn (S.Y.L.); guoyf@shanghaitech.edu.cn (Y.F.G.); xuzhang_fd@fudan.edu.cn (X.Z.)

Abstract

Altermagnets, recently proposed as a third category of collinear magnets, combine the features of zero net magnetization in antiferromagnets and the spin splitting in ferromagnets. While abundant spectroscopic evidence for altermagnetism has been reported, experimental observation of the anomalous Hall effect, a hallmark of ferromagnetism, remains scarce. Here, we present systematic measurements of the thermal Hall effect in two representative altermagnet candidates, MnTe and CrSb. In both materials, we observe a pronounced anomalous phonon thermal Hall signal, with no electrical counterpart observed, attributed to the coupling of this distinctive magnetic structure with phonons. Our findings establish the anomalous phonon thermal Hall effect as an intrinsic feature of altermagnets, and provide a sensitive probe to identify this new kind of quantum magnets.

Introduction

Collinear magnets are conventionally categorized into two main types: ferromagnets (FMs), where parallel spin alignment generates momentum-space band splitting and breaks time-reversal symmetry (TRS), and antiferromagnets (AFMs), in which antiparallel spin sublattices yield zero net magnetization. Recently, altermagnets (AMs) have been proposed as a third distinct form of collinear magnets, defined by alternating spin orientations in both real and reciprocal space, which combine characteristics of FMs and AFMs¹⁻⁴. In altermagnets, long-neglected nonmagnetic lattice atoms, e.g., Te in MnTe and Sb in CrSb (see Fig. 1a and Fig. 3a), play a crucial role: the spin space group symmetries allow magnetic sublattices to be connected solely through rotation or mirror operations, enabling spin splitting even in the absence of spin-orbit coupling (SOC) and a finite net magnetization^{1,2,5,6}.

Since the introduction of altermagnetism, several materials have been identified as potential altermagnets, with RuO₂ recognized as the first candidate predicted to exhibit the anomalous Hall effect (AHE) that arises from crystal TRS breaking⁷. Although nonlinear Hall signals have been observed in RuO₂/TiO₂ (110) films⁸, spin- and angle-resolved photoemission spectroscopy (ARPES) has not given any evidence for the expected spin splitting⁹, leaving the validity of the proposed altermagnetic order in rutile RuO₂ under scrutiny. More recently, spin splitting has been observed in CrSb¹⁰⁻¹³ and MnTe¹⁴⁻¹⁸, yet clear detection of anomalous Hall responses remains elusive¹⁹⁻²⁵. In CrSb, nonlinear Hall signals are attributed to multi-band effects¹⁹⁻²¹, whereas in MnTe, AHE hysteresis loops are not only very weak but also exhibit strong sample dependence²²⁻²⁵. Note that for RuO₂, saturation of the AHE is observed without zero-field AHE because of limitation by symmetry^{26,27}. Therefore, identifying genuine altermagnetic materials using multiple experimental techniques has become a key focus of current research.

Over past two decades, the thermal Hall effect (THE) in insulators has gained significant attention as a novel phenomenon²⁸⁻⁴⁴. According to these works, despite the absence of charge carriers, insulators subjected to a longitudinal temperature gradient

can still generate a transverse temperature difference in the presence of magnetic field. Distinct origins of the THE have been proposed, including magnons, various exotic excitations, and phonons. Most strikingly, such a THE has been observed in various trivial nonmagnetic insulators (including SiO₂, MgO and MgAlO₂) and semiconductors (including Si and Ge) with a scaling law of $|\kappa_{xy}| \sim \kappa_{xx}^2$, demonstrating a universal phonon THE (pTHE) in single crystals⁴⁵. In this context, many previous exotic interpretations may not be needed, but the underlying physics of this universal pTHE is still under investigation^{46,47}.

In magnetic materials, spin degree of freedom can significantly influence the pTHE, causing deviation from the quadratic scaling behavior⁴⁵. In collinear AFMs, the thermal Hall conductivity varies approximately linearly with magnetic field^{34–36,39,44}, similar to pTHE in nonmagnetic materials. By contrast, an anomalous THE has been observed in FMs^{29,32,38}, indicating spontaneous TRS breaking, while its origin—whether from magnons or phonons—remains unclear. Given the TRS breaking nature of AMs, it is of particular interest to examine whether the thermal Hall conductivity is anomalous in these materials.

In this Letter, we report systematic measurements of the THE in two representative altermagnet candidates, MnTe and CrSb. In semiconducting MnTe, where phonons dominate heat transport, we observe a pronounced anomalous thermal Hall response that far exceeds the electronic contribution estimated from the Wiedemann–Franz (WF) law. In metallic CrSb, after subtracting the electronic contribution, the remaining thermal Hall conductivity—primarily attributed to phonons—displays strong anomalous behavior. These results demonstrate the anomalous pTHE as a fundamental hallmark of altermagnetism, thus establishing phonon-mediated thermal transport as a superior probe to identify a new altermagnet—outperforming established electrical probing paradigms.

Results

The α -MnTe crystallizes in a NiAs-type structure ($P6_3/mmc$ #194; Fig. 1a) and

exhibits a compensated magnetic structure below the magnetic transition temperature $T_{AM} \approx 307$ K. The spins of Mn^{2+} ions are aligned parallel within the ab plane and anti-parallel along the c axis. The two sublattices with opposite spin orientations are interconnected by a sixfold rotation or a mirror operation, defining the symmetry of this altermagnetic phase. Figure 1b shows the temperature-dependent magnetic susceptibility of a MnTe single crystal (photo in the inset) measured from 2.1 to 350 K under zero-field cooling (ZFC) condition, revealing clear magnetic anisotropy below T_{AM} , consistent with the in-plane Néel vector. Furthermore, the isothermal magnetization $M(H)$ curves for $B \parallel c$, presented in Fig. 1c, are approximately linear at various temperatures, exhibiting typical antiferromagnetic behavior without any canted component.

Before measuring the thermal Hall effect, we have characterized the electrical transport properties of MnTe single crystal, as shown in Figs. 2a,b. The resistivity ρ_{xx} displays two distinct features: a sharp drop at T_{AM} , followed by an upturn below 60 K. The Hall conductivity σ_{xy} is positive, indicating that MnTe behaves as a p -type semiconductor. However, σ_{xy} varies linearly across the measured range, with no apparent anomalies, similar to some samples of Dai's group in Ref. 25. Figure 2c presents the thermal conductivity κ_{xx} which exhibits a pronounced phonon peak around 20 K. Notably, a thermal Hall signal has been observed in this material. The temperature-dependent total thermal Hall conductivity κ_{xy} follows the phonon peak in κ_{xx} , suggesting that phonons dominate heat transport in MnTe, as in various other materials^{37,41,43,45}. Unlike nonmagnetic and antiferromagnetic materials, κ_{xy} in MnTe exhibits a peculiar magnetic field dependence (Fig. 2d). As the magnetic field increases, κ_{xy} shows a hump around 1 T, followed by a sign reversal from positive to negative. This behavior is reminiscent of the electric anomalous Hall effect observed in many topological materials. The phonon thermal Hall conductivity κ_{xy}^{ph} is extracted by subtracting the carrier contribution using the WF Law, as shown in Fig. 2e. Due to the relatively small contribution of hole carriers in MnTe (from -0.9% at 10 K to -17.3% at 60 K), κ_{xy}^{ph} has a similar field dependence to the total thermal Hall conductivity. The phonon thermal Hall conductivity consists of two components: one is the conventional

part, which is linear in magnetic field, akin to that previously observed in nonmagnetic or collinear antiferromagnetic materials, and the other is the anomalous part. We fit the data using the following function⁴⁸:

$$\kappa_{xy}^{ph} = kB + \kappa_A \tanh(B/B_0). \quad (1)$$

The former linear term represents the conventional part, while the latter indicates the anomalous behavior, where k is the slope of the linear term, κ_A is the saturation value of the anomalous term, and $1/B_0$ is the differential permeability at $B = 0$ T. After subtracting the linear term, the anomalous pTHE is extracted and presented in Fig. 2f, analogous to the THE in FMs^{29,32,38}.

To examine whether the anomalous pTHE is a general feature of AMs, we turn to another altermagnetic candidate CrSb, which has a magnetic structure similar to that of α -MnTe and a transition temperature T_{AM} above 700 K. However, the spins of Cr^{2+} ions are aligned along the c axis (see Fig. 3a). Figure 3b presents the temperature-dependent magnetic susceptibility of a CrSb single crystal, measured from 1.8 to 300 K under ZFC condition. These data reveal distinct magnetic anisotropy, consistent with the out-of-plane Néel vector. The isothermal magnetization curves $M(H)$ for $B \parallel c$, shown in Fig. 3c, exhibit a small hysteresis and a weak ferromagnetic component with a saturation field near $B = 0.1$ T. This behavior differs from the out-of-plane response of MnTe but resembles its in-plane response, as shown in the Supplementary Fig. S2.

Similarly, we measured the electrical and thermal transport properties of the CrSb single crystal. As shown in Figs. 4a,b, ρ_{xx} exhibits clear metallic behavior with a residual resistivity ratio (RRR) of 4.41, indicating high sample quality. The negative Hall conductivity σ_{xy} confirms electron-dominated transport. In addition, σ_{xy} exhibits nonlinear field dependence across the entire temperature range, previously attributed to multiband effects¹⁹⁻²¹. The longitudinal thermal conductivity κ_{xx} of CrSb is plotted in Fig. 4c. After subtracting the electronic contribution calculated from the WF law, the phonon thermal conductivity reveals a broad peak around 40 K. This indicates a substantial electronic contribution to heat transport in metallic CrSb, in contrast to the phonon-dominated transport in MnTe. Figure 4d shows the total thermal Hall conductivity κ_{xy} of CrSb, which is sizable and exhibits a field dependence qualitatively

mirroring the electrical Hall behavior. To extract the phonon contribution and examine any anomalous component, we first subtract the electronic thermal Hall conductivity. At $T = 10$ K and $B = 9$ T, the total, electronic and phonon thermal Hall conductivities are -66.30 , -56.51 and -9.79 mW/(K m), respectively. The resulting phonon thermal Hall conductivity κ_{xy}^{ph} displays a robust signal. Furthermore, by subtracting the conventional linear-in-field part, as done for MnTe, the anomalous phonon thermal Hall conductivity is plotted in Fig. 4f. This anomalous κ_{xy}^{ph} of CrSb is remarkably similar to that observed in MnTe, including a saturation field and a magnitude that both increase with temperature. These findings provide compelling evidence for an intrinsic anomalous THE in CrSb, further supporting the presence of time-reversal symmetry breaking in AMs.

Discussion

The phonon thermal Hall effect has been widely observed in both magnetic and nonmagnetic materials. Except when the lattice thermal conductivity exhibits a strong magnetic-field dependence, the thermal Hall conductivity in the majority of materials is linear in magnetic field. This conventional linear-in-field thermal Hall response is also evident in MnTe and CrSb. Under a 9 T magnetic field, the temperature dependence of the extracted conventional phonon thermal Hall conductivity follows that of the lattice thermal conductivity, thereby providing strong support for this interpretation and underscoring the ubiquity of the conventional phonon thermal Hall effect. More importantly, once the electronic contribution is removed using the WF law, both materials exhibit a nonlinear phonon thermal Hall response, along with a field-induced sign reversal of the thermal Hall conductivity. To our knowledge, such behavior has not been reported previously in AMs. In fact, this anomalous phonon thermal Hall component has been observed only in ferromagnetic systems, such as $\text{Lu}_2\text{V}_2\text{O}_7$, $\text{Fe}_2\text{Mo}_3\text{O}_8$ and VI_3 ^{29,32,38}.

The linear-in-field contribution to κ_{xy} in MnTe and CrSb is consistent with the conventional pTHE, as widely reported in both magnetic and nonmagnetic materials³⁴⁻

37,39,41,44,45. In materials where the lattice thermal conductivity shows little field dependence, the phonon-derived κ_{xy} is expected to be strictly linear in B^{45} , and in our data the conventional phonon κ_{xy} extracted at 9 T closely follows the temperature dependence of the lattice thermal conductivity, supporting its assignment to the conventional pTHE.

After subtracting this conventional phonon background, a sizable residual anomalous κ_{xy}^{ph} remains, the field dependence of which is reminiscent of anomalous thermal Hall responses previously observed in ferromagnets^{29,32,38}. Small ferromagnetic signals have been reported for these altermagnet candidates^{22,49–51} (MnTe: in-plane; CrSb: out-of-plane) and are also present in our magnetization data. However, the saturation field of these weak ferromagnetic components (~ 0.1 T) is an order of magnitude smaller than the field scale required to saturate the anomalous κ_{xy}^{ph} (≥ 1 T). Because anomalous thermal Hall responses in ferromagnets typically track $M(H)^{29,32,38}$, this strong mismatch argues against weak net magnetization as the primary origin of the anomalous signal in MnTe and CrSb.

Mechanisms tied to the Néel vector and crystalline symmetry therefore provide a more natural explanation. In altermagnets, direction-dependent superexchange originating from the specific arrangement of nonmagnetic ligands breaks the combined time-reversal/spatial-translation protections that otherwise suppress Berry curvature. The same Berry-curvature physics that governs anomalous electrical Hall responses can couple to lattice degrees of freedom, producing an intrinsic “crystal” thermal Hall effect^{52,53} in which the magnitude and sign of the thermal Hall conductivity κ_{xy} are determined by the Néel vector rather than by any small net magnetization.

A closely related and plausible route is magnon–phonon hybridization. Hybridization between magnons and phonons in collinear ordered magnets can generate chiral phonon modes^{54–56}, thereby transferring magnetic Berry curvature to the phonon sector. Even when phonons dominate heat transport, the large thermal Hall signal has been attributed to phonon–magnon hybridization^{44,57}. A “magnon thermal Hall effect” has been proposed, in which the magnitude and sign of κ_{xy} are governed by

the Néel vector rather than by the net magnetization⁵³. Moreover, magnon–phonon hybridization has been observed experimentally in altermagnetic CoF₂⁵⁸. Against the expected background of spin–phonon interactions that renormalize phonon spectra at the Néel temperature, an additional strong coupling between a one-magnon excitation and the lowest-frequency Raman-active phonon of B_{1g} symmetry was reported⁵⁸. These hybrid quasiparticles possess finite phonon angular momentum opening the possibility of phononic counterparts to the electronic response effects in altermagnets⁵⁹. These findings provide a prerequisite for establishment the hybridization mechanism of THE, namely that phonon–magnon hybridization can imprint and substantially amplify an anomalous phonon κ_{xy} in altermagnets. In this scenario, a Néel-vector-driven crystal thermal Hall effect need not produce a large anomalous electrical Hall effect, and thus naturally accounts for the absence of AHE in CrSb^{19–21}, and for the sample-dependent AHE (very weak even if it presents) in MnTe^{22–25}.

To test this interpretation, we suggest more experiments: controlled rotation of the Néel vector (via magnetic field or strain) to track the symmetry and sign changes of κ_{xy} , high-resolution inelastic neutron or Raman/THz spectroscopy to resolve magnon–phonon anticrossings. Together, these probes can discriminate intrinsic Berry-curvature imprints on phonons from alternative extrinsic mechanisms and establish whether magnon–phonon hybridization is the dominant source of the anomalous thermal Hall response.

In summary, we have measured THE of two altermagnet candidates, semiconducting α -MnTe and metallic CrSb, and report the observation of a robust anomalous phonon κ_{xy} in both materials after subtracting the carrier and conventional phonon background. The observed field scales and magnetization behavior rule out weak ferromagnetism as the primary cause and point toward a Néel-vector- and lattice-symmetry-driven origin, possibly mediated or amplified by magnon–phonon coupling. Our results extend THE studies into altermagnets, highlight the important role phonons can play, and motivate further theoretical and experimental work to identify the microscopic mechanism.

Methods

Samples growth. MnTe single crystals were grown using an Sb-flux-assisted method. Starting materials, including Mn plates (99.9%, Macklin), Te powder (99.99%, Macklin), and Sb blocks (99.999%, Macklin), were placed in an alumina crucible with a molar ratio of Mn:Te:Sb = 1:1:20. To prevent oxidation, the crucible was sealed in a quartz ampoule under vacuum. The ampoule was then heated to 1050 °C over 15 h, held at that temperature for 10 h to ensure complete dissolution and homogenization, and subsequently cooled slowly at 2 °C/h to 700 °C. At this point, the excess Sb flux was efficiently removed by rapid centrifugation. The resulting black MnTe crystals exhibited shiny surfaces and typical dimensions of approximately $5 \times 4 \times 1 \text{ mm}^3$.

Single crystals of CrSb were grown using a chemical vapor transport method. Stoichiometric amounts of chromium powder (Cr, 99.5%, Macklin) and antimony blocks (Sb, 99.999%, Macklin) were mixed in a 1:1 molar ratio, with 0.1 g of iodine granules (I₂, 99.99%, Macklin) added as the transport agent. The mixture was loaded into a 14-cm-long quartz ampoule, which was then evacuated and sealed under vacuum. The sealed ampoule was placed horizontally in a two-zone tube furnace, with the source zone heated to 850 °C and the growth zone to 750 °C over 10 h. This temperature gradient was maintained for 150 h to facilitate crystal growth, after which the furnace was turned off and allowed to cool to room temperature. The resulting CrSb crystals were carefully extracted from the ampoule and rinsed with ethanol to remove residual iodine from their surfaces. Lustrous black plate-like crystals with typical dimensions of approximately $9 \times 7 \times 1 \text{ mm}^3$ were obtained.

Measurements. The VSM magnetization measurement was performed down to 2.1 K using a magnetic property measurement system (MPMS, Quantum Design). Samples for resistivity and thermal conductivity measurements were cut and polished into nearly rectangular shapes. The dimensions were $3.57 \times 1.43 \times 0.15 \text{ mm}^3$ for MnTe and $1.52 \times 1.14 \times 0.11 \text{ mm}^3$ for CrSb, respectively. The electrical and thermal transport measurements were conducted in a Physical Property Measurement system (PPMS,

Quantum Design) under high-vacuum environment. The heater and thermometers were connected to the sample by silver wires. The contacts were made of silver paint for MnTe and silver epoxy annealed at 120 °C for CrSb, respectively. Three-thermometers (Cernox 1050) method was employed to simultaneously measure the longitudinal and transverse thermal gradients. A constant heat current Q was applied along the x axis lying in the basal plane of the single crystal, using a resistive heater connected to one end of the sample, generating a longitudinal temperature difference $\Delta T_x = T_1 - T_2$ (Supplementary Fig. S1). The other end of the sample was attached to a heat sink with silver paint. The copper block is used as heat sink. The thermal conductivity along the x axis was calculated as $\kappa_{xx} = (Q/\Delta T_x)(L/wt)$. By applying a magnetic field B along the z directions, a transverse gradient $\Delta T_y = T_3 - T_2$ was generated. The thermal Hall conductivity was defined as $\kappa_{xy} = \kappa_{yy}(\Delta T_y/\Delta T_x)(L/w)$, where κ_{yy} is the longitudinal thermal conductivity along the y axis. We assumed $\kappa_{yy} = \kappa_{xx}$ for crystals with high symmetry. The contamination from κ_{xx} in κ_{xy} due to contact misalignment is removed by performing field anti-symmetrization of the transverse temperature difference ΔT_y , i.e. $\Delta T_y = [\Delta T_y(H) - \Delta T_y(-H)]/2$. The positive direction of magnetic field is illustrated by blue arrows in Supplementary Fig. S1.

Data availability

The data that support the findings of this study are available from the corresponding author upon reasonable request.

References

1. Šmejkal, L., Sinova, J. & Jungwirth, T. Beyond Conventional Ferromagnetism and Antiferromagnetism: A Phase with Nonrelativistic Spin and Crystal Rotation Symmetry. *Phys. Rev. X* **12**, 031042 (2022).
2. Šmejkal, L., Sinova, J. & Jungwirth, T. Emerging Research Landscape of Altermagnetism. *Phys. Rev. X* **12**, 040501 (2022).
3. Song, C. *et al.* Altermagnets as a new class of functional materials. *Nat. Rev. Mater.* **10**, 473 (2025).
4. Jungwirth, T. *et al.* Symmetry, microscopy and spectroscopy signatures of altermagnetism. *Nature* **649**, 837 (2026).
5. Ma, H.-Y. *et al.* Multifunctional antiferromagnetic materials with giant piezomagnetism and noncollinear spin current. *Nat. Commun.* **12**, 2846 (2021).
6. Liu, P., Li, J., Han, J., Wan, X. & Liu, Q. Spin-Group Symmetry in Magnetic Materials with Negligible Spin-Orbit Coupling. *Phys. Rev. X* **12**, 021016 (2022).
7. Šmejkal, L., González-Hernández, R., Jungwirth, T. & Sinova, J. Crystal time-reversal symmetry breaking and spontaneous Hall effect in collinear antiferromagnets. *Sci. Adv.* **6**, eaaz8809 (2020).
8. Feng, Z. *et al.* An anomalous Hall effect in altermagnetic ruthenium dioxide. *Nat. Electron.* **5**, 735 (2022).
9. Liu, J. *et al.* Absence of Altermagnetic Spin Splitting Character in Rutile Oxide RuO₂. *Phys. Rev. Lett.* **133**, 176401 (2024).
10. Ding, J. *et al.* Large Band Splitting in g-Wave Altermagnet CrSb. *Phys. Rev. Lett.* **133**, 206401 (2024).
11. Reimers, S. *et al.* Direct observation of altermagnetic band splitting in CrSb thin films. *Nat. Commun.* **15**, 2116 (2024).
12. Li, C. *et al.* Topological Weyl altermagnetism in CrSb. *Commun. Phys.* **8**, 311 (2024).
13. Liao, S. *et al.*, Direct Observation of Large Altermagnetic Splitting in CrSb (100) Thin Film. *Chin. Phys. Lett.* **42**, 067503 (2025).
14. Krempaský, J. *et al.* Altermagnetic lifting of Kramers spin degeneracy. *Nature* **626**, 517 (2024).
15. Lee, S. *et al.* Broken Kramers Degeneracy in Altermagnetic MnTe. *Phys. Rev. Lett.* **132**, 036702 (2024).
16. Liu, Z., Ozeki, M., Asai, S., Itoh, S. & Masuda, T. Chiral Split Magnon in Altermagnetic MnTe. *Phys. Rev. Lett.* **133**, 156702 (2024).
17. Osumi, T. *et al.* Observation of a giant band splitting in altermagnetic MnTe. *Phys. Rev. B* **109**, 115102 (2024).
18. Zhang, T. *et al.* Evidence for Itinerant Electron-Local Moment Interaction in Li-Doped α -MnTe. *arXiv: 2512.00747* (2025).
19. Urata, T., Hattori, W. & Ikuta, H. High mobility charge transport in a multicarrier altermagnet CrSb. *Phys. Rev. Mater.* **8**, 084412 (2024).
20. Bai, Y. *et al.* Nonlinear field dependence of Hall effect and high-mobility multi-carrier transport in an altermagnet CrSb. *Appl. Phys. Lett.* **126**, 042402 (2025).

21. Peng, X. *et al.* Scaling behavior of magnetoresistance and Hall resistivity in the altermagnet CrSb. *Phys. Rev. B* **111**, 144402 (2025).
22. Wasscher, J. D. Evidence of weak ferromagnetism in MnTe from galvanomagnetic measurements. *Solid State Commun.* **3**, 169 (1965).
23. Gonzalez Betancourt, R. D. *et al.* Spontaneous Anomalous Hall Effect Arising from an Unconventional Compensated Magnetic Phase in a Semiconductor. *Phys. Rev. Lett.* **130**, 036702 (2023).
24. Kluczyk, K. P. *et al.* Coexistence of anomalous Hall effect and weak magnetization in a nominally collinear antiferromagnet MnTe. *Phys. Rev. B* **110**, 155201 (2024).
25. Liu, Z. *et al.* Strain-Tunable Anomalous Hall Effect in Hexagonal MnTe. *arXiv*: 2509.19582 (2025).
26. Tschirner, T. *et al.* Saturation of the anomalous Hall effect at high magnetic fields in altermagnetic RuO₂. *APL Mater.* **11**, 101103 (2023).
27. Jeong, S. G. *et al.* Metallicity and anomalous Hall effect in epitaxially strained, atomically thin RuO₂ films. *Proc. Natl. Acad. Sci. U.S.A.* **122**, e2500831122 (2025).
28. Strohm, C., Rikken, G. L. J. A. & Wyder, P. Phenomenological Evidence for the Phonon Hall Effect. *Phys. Rev. Lett.* **95**, 155901 (2005).
29. Onose, Y. *et al.* Observation of the Magnon Hall Effect. *Science* **329**, 297 (2010).
30. Hirschberger, M., Chisnell, R., Lee, Y. S. & Ong, N. P. Thermal Hall Effect of Spin Excitations in a Kagome Magnet. *Phys. Rev. Lett.* **115**, 106603 (2015).
31. Hirschberger, M., Krizan, J. W., Cava, R. J. & Ong, N. P. Large thermal Hall conductivity of neutral spin excitations in a frustrated quantum magnet. *Science* **348**, 106 (2015).
32. Ideue, T., Kurumaji, T., Ishiwata, S. & Tokura, Y. Giant thermal Hall effect in multiferroics. *Nat. Mater.* **16**, 797 (2017).
33. Kasahara, Y. *et al.* Majorana quantization and half-integer thermal quantum Hall effect in a Kitaev spin liquid. *Nature* **559**, 227 (2018).
34. Grissonnanche, G. *et al.* Giant thermal Hall conductivity in the pseudogap phase of cuprate superconductors. *Nature* **571**, 376 (2019).
35. Grissonnanche, G. *et al.* Chiral phonons in the pseudogap phase of cuprates. *Nat. Phys.* **16**, 1108 (2020).
36. Boulanger, M.-E. *et al.* Thermal Hall conductivity in the cuprate Mott insulators Nd₂CuO₄ and Sr₂CuO₂Cl₂. *Nat. Commun.* **11**, 5325 (2020).
37. Li, X., Fauqué, B., Zhu, Z. & Behnia, K. Phonon Thermal Hall Effect in Strontium Titanate. *Phys. Rev. Lett.* **124**, 105901 (2020).
38. Zhang, H. *et al.* Anomalous Thermal Hall Effect in an Insulating van der Waals Magnet. *Phys. Rev. Lett.* **127**, 247202 (2021).
39. Chen, L., Boulanger, M.-E., Wang, Z.-C., Tafti, F. & Taillefer, L. Large phonon thermal Hall conductivity in the antiferromagnetic insulator Cu₃TeO₆. *Proc. Natl. Acad. Sci. U.S.A.* **119**, e2208016119 (2022).
40. Gillig, M. *et al.* Phononic-magnetic dichotomy of the thermal Hall effect in the Kitaev material Na₂Co₂TeO₆. *Phys. Rev. Res.* **5**, 043110 (2023).
41. Li, X. *et al.* The phonon thermal Hall angle in black phosphorus. *Nat. Commun.* **14**, 1027 (2023).

42. Ataei, A. *et al.* Phonon chirality from impurity scattering in the antiferromagnetic phase of Sr₂IrO₄. *Nat. Phys.* **20**, 585–588 (2024).
43. Sharma, R., Valldor, M. & Lorenz, T. Phonon thermal Hall effect in nonmagnetic Y₂Ti₂O₇. *Phys. Rev. B* **110**, L100301 (2024).
44. Meng, Q. *et al.* Thermodynamic Origin of the Phonon Hall Effect in a Honeycomb Antiferromagnet. *arXiv:2403.13306* (2024).
45. Jin, X. B. *et al.* Discovery of Universal Phonon Thermal Hall Effect in Crystals. *Phys. Rev. Lett.* **135**, 196302 (2025).
46. Behnia, K. Phonon thermal Hall as a lattice Aharonov-Bohm effect. *SciPost Phys. Core* **8**, 061 (2025).
47. Oh, T. Thermal Hall Effect Induced by Phonon Skew-Scattering via Orbital Magnetization. *arXiv:2507.22436* (2025).
48. Chen, X., Xie, H., Shen, H. & Wu, Y. Vector Magnetometer Based on a Single Spin-Orbit-Torque Anomalous-Hall Device. *Phys. Rev. Appl.* **18**, 024010 (2022).
49. Kim, W. *et al.* Room-Temperature Ferromagnetic Property in MnTe Semiconductor Thin Film Grown by Molecular Beam Epitaxy. *IEEE Trans. Magn.* **45**, 2424 (2009).
50. Zhou, Z. *et al.* Manipulation of the altermagnetic order in CrSb via crystal symmetry. *Nature* **638**, 645 (2025).
51. Tseng, C.-H. *et al.* Epitaxial Growth of Altermagnet CrSb via Magnetron Sputtering. *Cryst. Growth Des.* **25**, 9171 (2025).
52. Zhou, X. *et al.* Crystal Thermal Transport in Altermagnetic RuO₂. *Phys. Rev. Lett.* **132**, 056701 (2024).
53. Hoyer, R., Jaeschke-Ubiergo, R., Ahn, K.-H., Šmejkal, L. & Mook, A. Spontaneous crystal thermal Hall effect in insulating altermagnets. *Phys. Rev. B* **111**, L020412 (2025).
54. Nomura, T. *et al.* Phonon Magneto-chiral Effect. *Phys. Rev. Lett.* **122**, 145901 (2019).
55. Thingstad, E., Kamra, A., Brataas, A. & Sudbø, A. Chiral Phonon Transport Induced by Topological Magnons. *Phys. Rev. Lett.* **122**, 107201 (2019).
56. Cui, J. *et al.* Chirality selective magnon-phonon hybridization and magnon-induced chiral phonons in a layered zigzag antiferromagnet. *Nat. Commun.* **14**, 3396 (2023).
57. Yang, H., Go, G., Park, J., Kim, S. K. & Park, J.-G. Exchange striction induced thermal Hall effect in the van der Waals antiferromagnet MnPS₃. *Phys. Rev. B* **110**, 165147 (2024).
58. Prosnikov, M. A., Bal, M., Pisarev, R. V., Christianen, P. C. M. & Kalashnikova, A. M. Giant Intrinsic Nonlinear Phonon-Magnon Coupling in the Antiferromagnet CoF₂. *arXiv:2405.07304* (2024).
59. Bendin, H., Mook, A., Mertig, I. & Neumann, R. R. D-Wave Phonon Angular Momentum Texture in Altermagnets by Magnon-Phonon-Hybridization. *arXiv:2511.08357* (2026).

Acknowledgements

This work is supported by the Natural Science Foundation of China (Grant No. 12534004), the Shanghai Municipal Science and Technology Major Project (Grant No. 2019SHZDZX01), and Quantum Science and Technology-National Science and Technology Major Project (Grant No. 2024ZD0300104). Y.F.G. acknowledges the National Key R&D Program of China (Grants No. 2024YFA1408400 and 2023YFA140610) and the open research fund of Beijing National Laboratory for Condensed Matter Physics (2023BNLCMPKF002).

Author Contributions

S.Y.L. and X.Z. conceived the idea and designed the experiments. Y.X.L and Y.F.G. grew the MnTe and CrSb samples. W.B.W. and X.Z. performed the measurements. W.B.W., X.Z. and S.Y.L. analyzed the data. W.B.W, X.Z. and S.Y.L. wrote the paper with assistance from all the authors. W.B.W, X.Z. contributed equally to this work.

Competing interests

The authors declare no competing interests.

Additional Information

Supplementary information is available for this paper at URL inserted when published.

Correspondence and requests for materials should be addressed to S.Y.L. (shiyang_li@fudan.edu.cn) and X.Z. (xuzhang_fd@fudan.edu.cn).

Figure 1

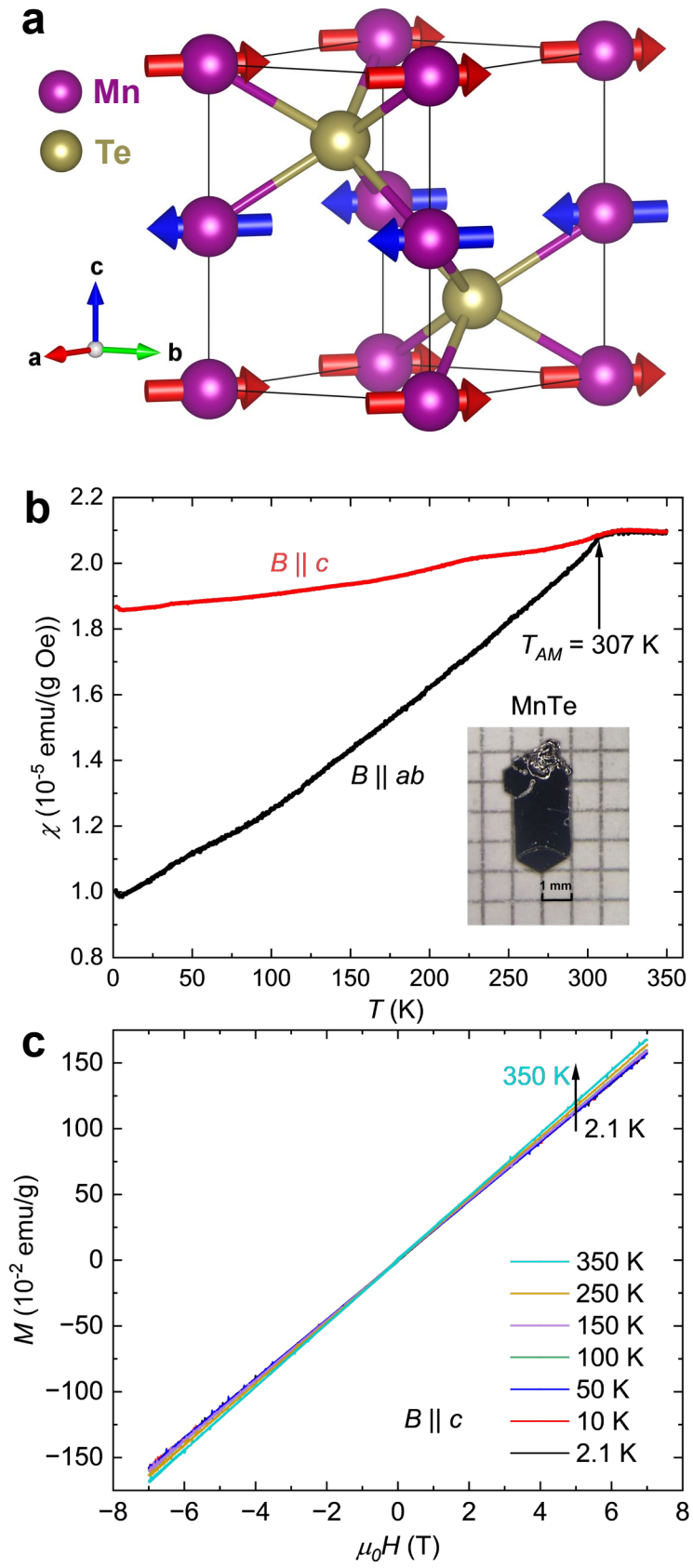


Figure 2

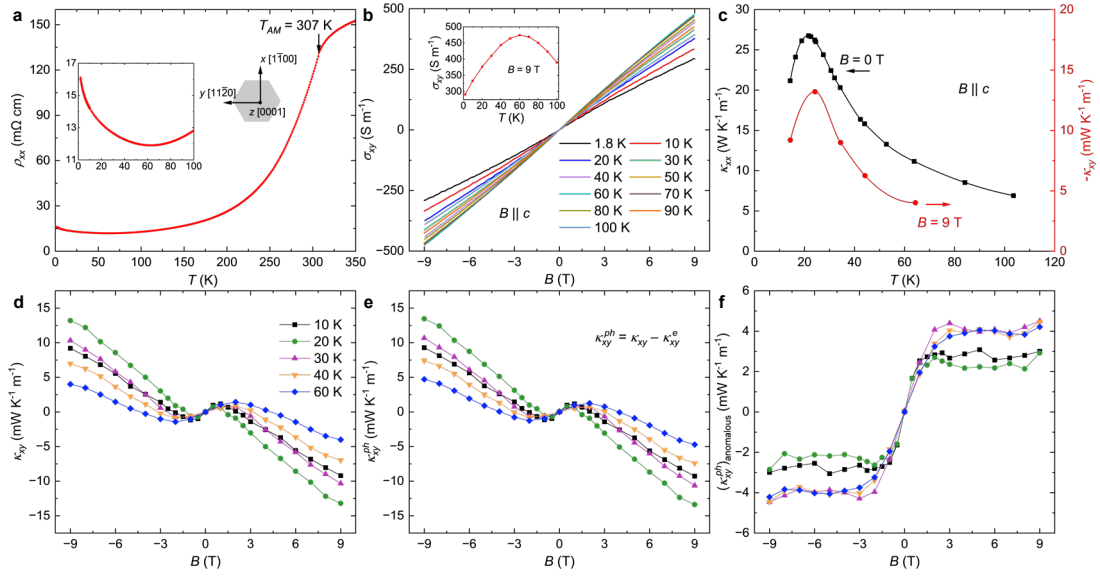


Figure 3

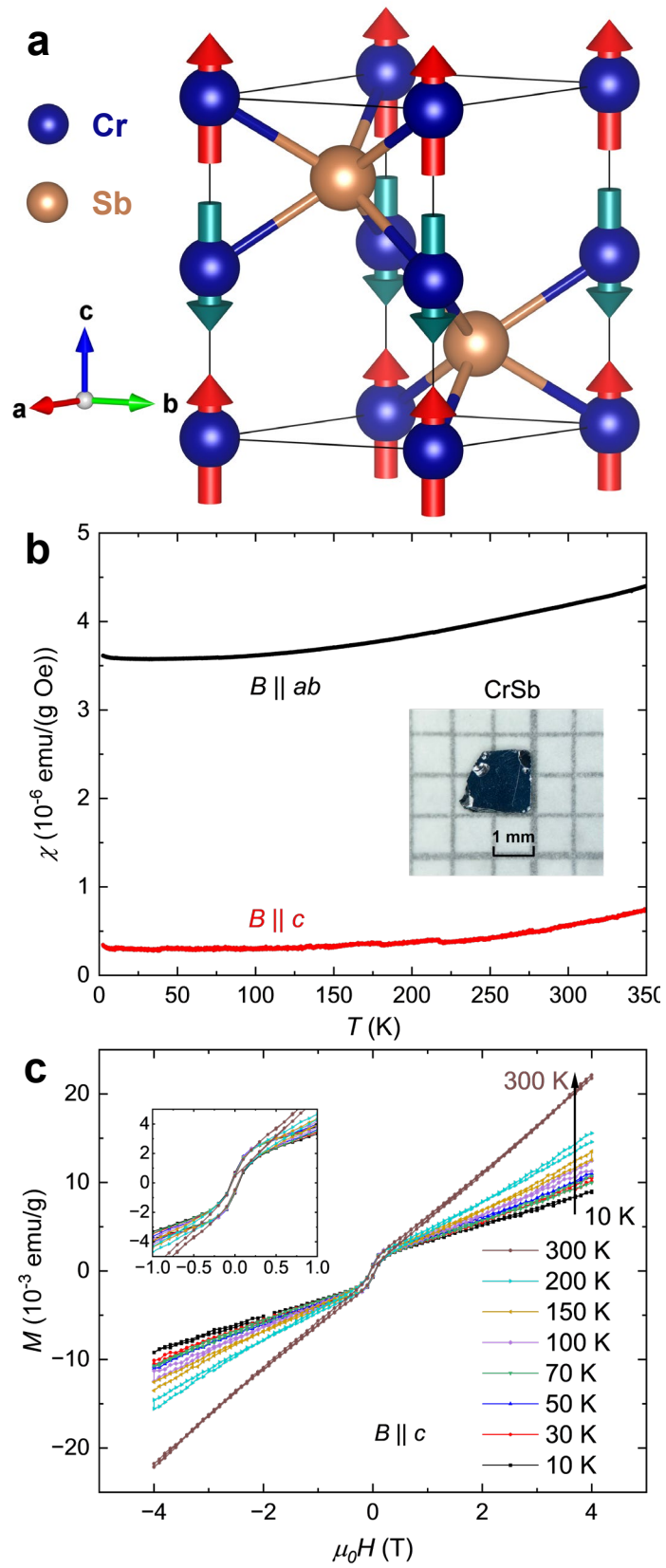


Figure 4

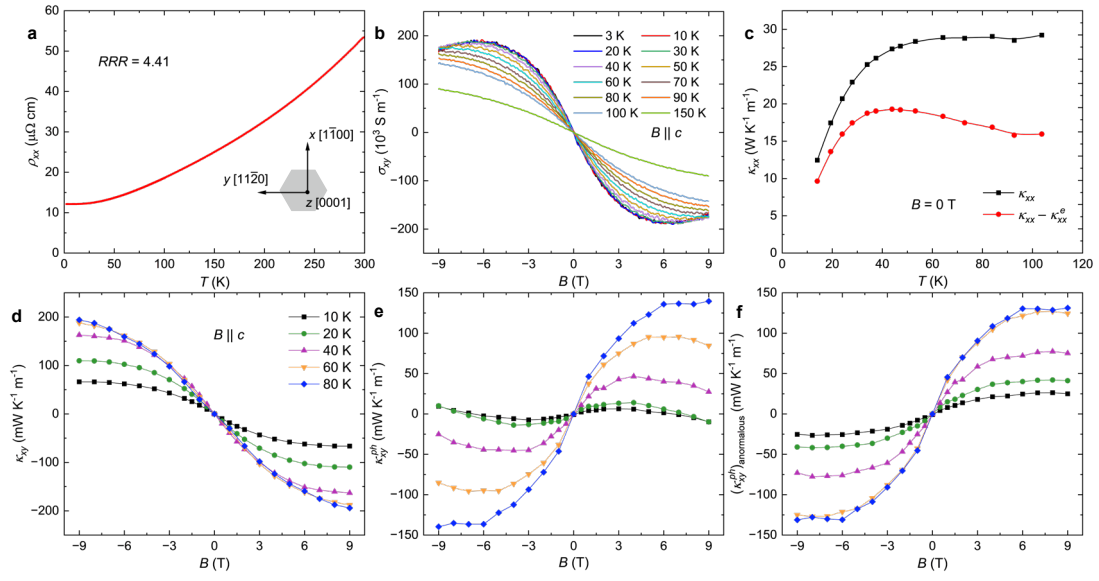


Figure captions

Figure 1 | Crystal structure and magnetization of α -MnTe. **a**, The crystal structure of α -MnTe with opposite-spin sublattices. **b**, Temperature-dependent magnetic susceptibility measured under ZFC conditions for different magnetic-field directions. The inset shows an optical image of the MnTe crystal used for the measurements. **c**, Field-dependent magnetization at different temperatures for $B \parallel c$.

Figure 2 | Electrical and thermal transport in α -MnTe. **a**, In-plane longitudinal resistivity of a α -MnTe single crystal in zero field. The left inset shows an enlarged view of the low-temperature region. The right inset defines specific crystalline orientations in the hexagonal crystal. **b**, Field-dependent Hall conductivity at different temperatures for $B \parallel c$. The inset presents the temperature-dependence of Hall conductivity at $B = 9$ T. **c**, Temperature-dependent longitudinal ($B = 0$ T) and transverse ($B = 9$ T) thermal conductivities. **d, e, f** Field-dependent total, phonon and anomalous thermal Hall conductivities at different temperatures for $B \parallel c$.

Figure 3 | Crystal structure and magnetization of CrSb. **a**, The crystal structure of hexagonal CrSb with opposite-spin sublattices. **b**, Temperature-dependent magnetic susceptibility under ZFC conditions for different magnetic-field directions. The inset shows an optical image of the CrSb crystal used for experiments. **c**, Field-dependent magnetization at various temperatures for $B \parallel c$. The inset presents an enlarged view of the low-field region.

Figure 4 | Electrical and thermal transport in CrSb. **a**, In-plane longitudinal resistivity of a CrSb single crystal in zero field. The inset defines specific crystalline orientations in the hexagonal crystal. **(b)** Field-dependent Hall conductivity at different temperatures for $B \parallel c$. **(c)** Temperature-dependent total and phonon-only longitudinal thermal conductivities at $B = 0$ T. **d, e, f** Field-dependent total, phonon and anomalous thermal Hall conductivities at different temperatures for $B \parallel c$.

Supplementary Information for
“Observation of anomalous thermal Hall effect in altermagnets”

Wenbo Wan^{1,2*}, Xu Zhang^{1*✉}, Yixuan Luo³, Yanfeng Guo^{3,4,✉} and Shiyan Li^{1,2,5,6,✉}

¹State Key Laboratory of Surface Physics, and Department of Physics, Fudan University, Shanghai 200438, China

²Shanghai Research Center for Quantum Sciences, Shanghai 201315, China

³State Key Laboratory of Quantum Functional Materials, School of Physical Science and Technology, ShanghaiTech University, Shanghai 201210, China

⁴ShanghaiTech Laboratory for Topological Physics, ShanghaiTech University, Shanghai 201210, China

⁵Shanghai Branch, Hefei National Laboratory, Shanghai 201315, China

⁶Collaborative Innovation Center of Advanced Microstructures, Nanjing 210093, China

Corresponding author. Email: shiyan_li@fudan.edu.cn (S.Y.L.); guoyf@shanghaitech.edu.cn (Y.F.G.); xuzhang_fd@fudan.edu.cn (X.Z.)

Supplementary Note 1: Setup of thermal transport measurement.

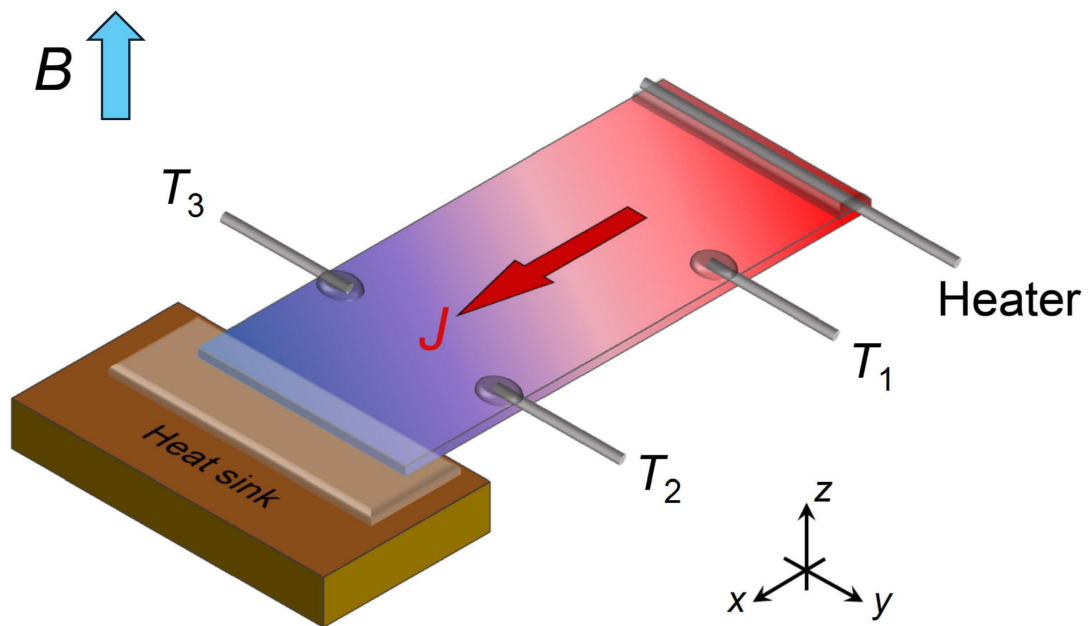


Figure S1 | Setup of thermal transport measurement.

Supplementary Note 2: In-plane $M(H)$ curves of MnTe.

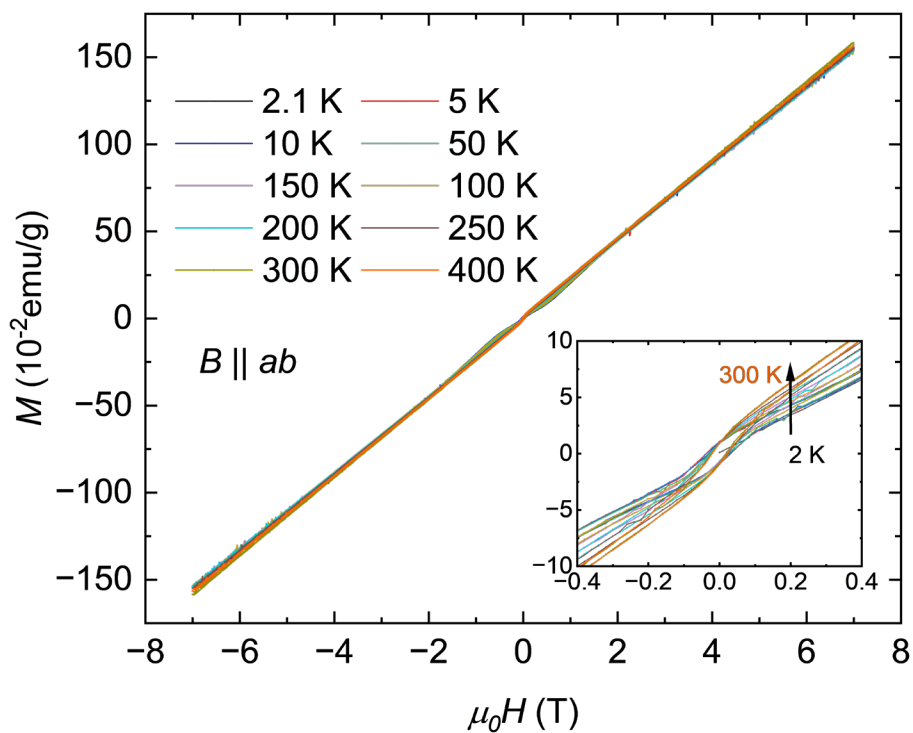


Figure S2 | In-plane $M(H)$ curves of MnTe. Field-dependent magnetization of MnTe at different temperatures for $B \parallel ab$. The inset presents an enlarged view of the low-field region.